8.1 Introduction

Rare earth (RE) substitution in the M-type hexaferrite has grown up significantly over several years. Doping of RE ion into strontium hexaferrite improves not only the magneto-crystalline anisotropy (MCA), but also improves the electro-magnetic properties [Luo *et al*. (2015)]. RE ions have 4f unpaired electrons, and they have strong couplings of 4f–3d angular momentum, which improves the electro-magnetic properties. Meanwhile, the 4f shell is shielded by $5s^2\ 5p^6$ and almost it is not affected by the potential field of nearby ions leading to the enrichment of the coupling. Many trials have been made on RE ion substitution. Among them, Liu *et al*. (2002a) have reported that La^{+3} doping in Sr hexaferrite has remarkably increased the saturation magnetization (M_s), and intrinsic coercivity (iH_c). Grossinger *et al*. (2003) have reported that Sm^{+3} substitution in Sr hexaferrite increased the coercivity by 18%. The increase in H_c in the permanent ferrites is dependent on the anisotropy constant (k_{eff}), which is affected by ionic interaction in the crystal lattice, and by doping [Kools *et al*. (2002)].

In this work, La^{+3} & Sm^{+3} substituted strontium hexaferrite, $SrAl_4(La_{0.5}Sm_{0.5})_xFe_{8-x}O_{19}$ with x = 0.0, 0.5, 1.0, & 1.5, have been synthesized by the auto combustion method, as discussed in section 3.1.1. Rietveld structure refinement is carried out to estimate crystallite size, strain, and variation in lattice parameters with composition. The substitution effect of RE elements on structural, microstructure evolution, dielectric, and magneto-electrical properties of the ferrites have been investigated.

8.2 Results and Discussion

The FTIR spectra of calcined dried powders for various compositions are shown in Figure 8.1. It shows that the characteristic bands are appeared in the range of 650-550 cm^{-1},

and 500-400 cm^{-1}. The two main wide metal oxygen bonds of ferrites have been found, the low-frequency band (υ_1) around 500-400 cm^{-1} is ascribed to intrinsic stretching vibrations of the metal cation at the octahedral site, while the higher frequency band (υ_2) around 650-550 cm^{-1} is attributed to the intrinsic stretching vibrations of the metal cation at the tetrahedral site. The bands are appeared due to the ion vibrations in the crystal lattice. The absorption band 637 cm^{-1}, 579 cm^{-1} are recognized to the tetrahedral stretching vibration of Fe-O in crystal lattice [Thakur *et al.* (2012)], and band around 445 cm^{-1} is known as stretching vibration of metal-oxygen bond suggesting the formation of hexaferrite [Mali and Ataie (2005)]. From these IR spectra, it is found that there are no other peaks at higher frequency band. The absence of the higher frequency band suggests the finishing of the redox reaction for hexaferrite formation.
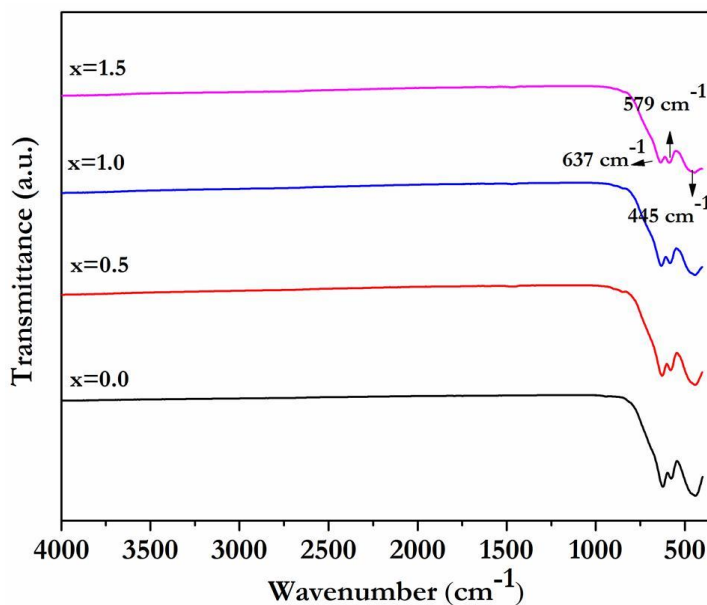

Figure 8.1 FTIR spectra of calcined $SrAl_4Fe_{(8-x)}(La_{0.5}Sm_{0.5})_xO_{19}$ ferrite powders.

Figure 8.2 shows the XRD pattern of substituted $SrAl_4(La_{0.5}Sm_{0.5})_xFe_{8-x}O_{19}$ ($0.0 \leq x \leq$ 1.5) ferrites. All the XRD patterns exhibit the characteristic peaks similar to the strontium

hexaferrite JCPDS # 720739 [Debnath *et al*. (2015)] suggesting the formation of phase similar to strontium hexaferrite for doped samples also. In addition, few peaks marked by an asterisk "*" are also observed for x = 1.5 samples, it is recognized to traces of samarium ferrite [Cui *et al*. (2014)]. Further, the peak corresponding to the hexaferrite phase in the XRD patterns, shifts to the lower angle with increasing La-Sm substitution suggesting an increase in the lattice parameters (LP), and unit cell volume. This is a usual observation as the ionic radius of the RE ions is bigger than the Fe^{+3} ion, and therefore cell expansion is expected. The substitution of RE leads to the change in the peak intensities, and broadening which can be ascribed to crystallite size, and lattice strain effects. For x = 1.5, the peak shifts towards higher angle, i.e., shrinkage in the lattice, may be due to the enhancing internal compressive strain (shown in Table 8.1) with the increase in Sm content [Wang *et al*. (2015)].
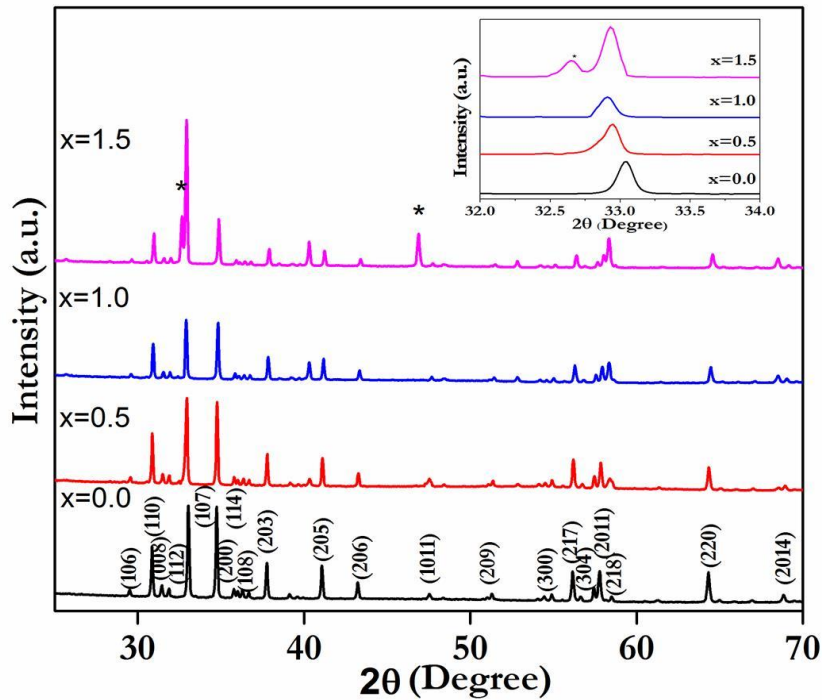

Figure 8.2 XRD analysis of sintered $SrAl_4Fe_{(8-x)}(La_{0.5}Sm_{0.5})_xO_{19}$ ferrites.

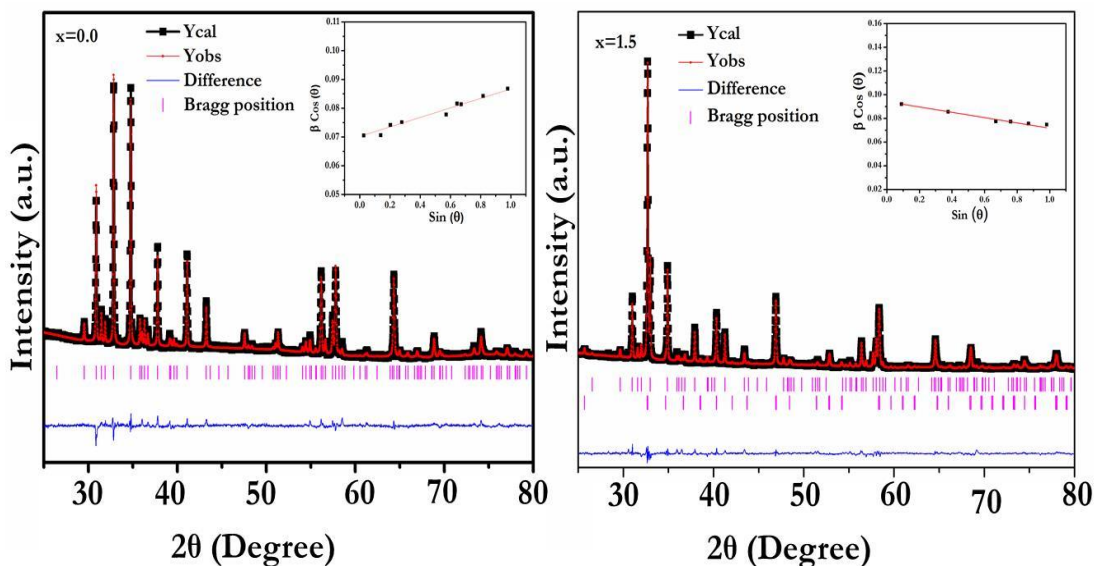**Figure 8.3** Rietveld refined XRD pattern of sintered $SrAl_4Fe_{(8-x)}(La_{0.5}Sm_{0.5})_xO_{19}$ ferrites with x = 0.0 and 1.5.

The structure of various compositions of $SrAl_4(La_{0.5}Sm_{0.5})_xFe_{8-x}O_{19}$ ($0.0 \leq x \leq 1.5$) ferrite is also analyzed by Rietveld structure refinement using *P63/mmc* space group reported for undoped $SrAl_4Fe_8O_{19}$ hexaferrite. The experimentally observed, Rietveld calculated and their difference XRD patterns for $SrAl_4Fe_8O_{19}$, and $SrAl_4(La_{0.5}Sm_{0.5})_{1.5}Fe_{6.5}O_{19}$ obtained by Rietveld refinement are shown in Figure 8.3. Rietveld refinement confirms that all peaks are related to the M-type hexagonal structure with *P63/mmc* space group for $SrAl_4Fe_8O_{19}$. For $SrAl_4(La_{0.5}Sm_{0.5})_{1.5}Fe_{6.5}O_{19}$, since $SmFeO_3$ phase is also present with the hexaferrite phase, two-phase refinement is carried out considering coexistence of both phases. As reported by earlier authors [Kuo *et al*. (2014)], *Pbnm* space group is used to refine the structure of the $SmFeO_3$. The Rietveld fitting for this composition is also very good. The fitted patterns are in a good matching with the experimental data indicating the better quality of the results.

The structural & refining parameters, micro-strain, c/a ratio, and the average size of the crystallites are given in Table 8.1 & Table 8.2. The experimental XRD broadening is related to both size, and lattice strain effects. It can be appropriately characterized by the Williamson-Hall (W-H) equation, as discussed in section 3.15.

Table 8.1 Lattice parameter, R_p, R_{wp}, χ^2, strain, c/a ratio, and crystallite size, of

$SrAl_4(La_{0.5}Sm_{0.5})_xFe_{8-x}O_{19}$ ferrites.

Composition	Lattice parameter (Å)		R_p (%)	R_{wp} (%)	χ^2	Strain	c/a	Crystallite size (nm)
	(a)	*(c)*						
x = 0.0	5.78	22.72	2.06	2.65	1.65	0.00413	3.93	12.64
x = 0.5	5.80	22.75	2.85	3.80	1.80	0.00673	3.92	14.27
x = 1.0	5.82	22.87	3.62	5.09	2.11	0.01270	3.92	19.98
x = 1.5	5.76	22.63	3.85	5.21	2.13	-0.03740	3.92	14.53

Williamson-Hall plots for the $SrAl_4Fe_8O_{19}$, and $SrAl_4(La_{0.5}Sm_{0.5})_{1.5}Fe_{6.5}O_{19}$ ferrite nano particles are given in the insets of Figure 8.3. W-H plot shows a linear fit, and positive slope for x = 0.0 composition, and negative slope for x = 1.5 specimen. Positive slope represents to tensile strain for the composition up to x = 1.0, and negative slope represents to compressive strain for x = 1.5 composition. Presence of positive strain is appearing due to the RE ions in the lattice [Rana *et al.* (2016)]. With increase in the substitution, it results to a monotonic increase in strain. This strain is accountable for an increment in crystallite size, because larger tensile strain results to the extension of crystal. The compressive strain for x =

1.5 composition may be due to the impurity phase (SmFeO$_3$) or defects, and inequality in the

assigning of some atoms at their sites during growth of the ferrite [Rana *et al*. (2016)].

Table 8.2 Rietveld refined structural parameters of SrAl$_4$(La$_{0.5}$Sm$_{0.5}$)$_x$Fe$_{8-x}$O$_{19}$ hexaferrites.

Composition	Sites	x	y	z	Occ.
SrFe$_8$Al$_4$O$_{19}$	Sr (*2d*)	0.6667	0.3333	0.2500	1
	Fe1(*2a*)	0.0000	0.0000	0.0000	1
	Fe2(2b)	0.0000	0.0000	0.2531	1
	Fe3(*4f₁*)	0.3333	0.6667	0.0282	2
	Fe4(*4f₂*)	0.3333	0.6667	0.1900	2
	Fe5(*12k*)	0.1683	0.3366	-0.1083	2
	Al(*12k*)	0.1683	0.3366	-0.1083	4
	O1(*4e*)	0.0000	0.0000	0.1480	2
	O2 (*4f*)	0.3333	0.6667	-0.0564	2
	O3 (*6h*)	0.1830	0.3650	0.2500	3
	O4 (*12k*)	0.1552	0.3101	0.0505	6
	O5 (*12k*)	0.5060	0.0110	0.1477	6
Sr Al$_4$(La$_{0.5}$Sm$_{0.5}$)$_{0.5}$Fe$_{7.5}$O$_{19}$	Sr (*2d*)	0.6667	0.3333	0.2500	1
	Fe1(*2a*)	0.0000	0.0000	0.0000	1
	Fe2(*2b*)	0.0000	0.0000	0.2531	1
	Fe3(*4f₁*)	0.3333	0.6667	0.0269	2
	Fe4(*4f₂*)	0.3333	0.6667	0.1900	1.5
	La(*4f₂*)	0.3333	0.6667	0.1900	0.25
	Sm(*4f₂*)	0.3333	0.6667	0.1900	0.25
	Fe5(*12k*)	0.1593	0.3189	-0.1084	2
	Al(*12k*)	0.1593	0.3189	-0.1084	4
	O 1(*4e*)	0.0000	0.0000	0.1580	2

	O2 (*4f*)	0.3333	0.6667	-0.0545	2
	O3 (*6h*)	0.1836	0.3672	0.2500	3
	O4 (*12k*)	0.1778	0.3556	0.0532	6
	O5 (*12k*)	0.5080	0.0162	0.1487	6
Sr Al$_4$(La$_{0.5}$Sm$_{0.5}$)$_{1.0}$Fe$_{7.0}$O$_{19}$	Sr (*2d*)	0.6667	0.3333	0.2500	1
	Fe1(*2a*)	0.0000	0.0000	0.0000	1
	Fe2(*2b*)	0.0000	0.0000	0.2531	1
	Fe3(*4f₁*)	0.3333	0.6667	0.0275	2
	Fe4(*4f₂*)	0.3333	0.6667	0.1880	1.0
	La(*4f₂*)	0.3333	0.6667	0.1880	0.5
	Sm(*4f₂*)	0.3333	0.6667	0.1880	0.5
	Fe5(*12k*)	0.1630	0.3259	-0.1071	2
	Al(*12k*)	0.1630	0.3259	-0.1071	4
	O 1(*4e*)	0.0000	0.0000	0.1680	2
	O2 (*4f*)	0.3333	0.6667	-0.0565	2
	O3 (*6h*)	0.1512	0.3025	0.2500	3
	O4 (*12k*)	1.1743	0.3488	0.0529	6
	O5 (*12k*)	0.4935	-0.0126	0.1430	6
SrAl$_4$(La$_{0.5}$Sm$_{0.5}$)$_{1.5}$Fe$_{6.5}$O$_{19}$	Sr (*2d*)	0.6667	0.3333	0.2500	1
	Fe1(*2a*)	0.0000	0.0000	0.0000	1
	Fe2(*2b*)	0.0000	0.0000	0.2531	1
	Fe3(*4f₁*)	0.3333	0.6667	0.0197	2
	Fe4(*4f₂*)	0.3333	0.6667	0.1877	0.5
	La(*4f₂*)	0.3333	0.6667	0.1877	0.75
	Sm(*4f₂*)	0.3333	0.6667	0.1877	0.75
	Fe5(*12k*)	0.1617	0.3236	-0.1121	2

	Al(*12k*)	0.1617	0.3236	-0.1121	4
	O 1(*4e*)	0.0000	0.0000	0.1846	2
	O2 (*4f*)	0.3333	0.6667	-0.1877	2
	O3 (*6h*)	0.1406	0.2814	0.25000	3
	O4 (*12k*)	0.1937	0.3873	0.0468	6
	O5 (*12k*)	0.5181	-0.0362	0.1534	6
SmFeO$_3$ (Secondary phase at x=1.5)	Sm (*4c*)	1.0123	0.0244	0.2500	1
	O1(*8d*)	0.7683	0.2909	-0.0001	2
	O2(*4c*)	-0.0241	0.5058	0.2500	1
	Fe(*4b*)	0.0000	0.5000	0.0000	1

As reported in Table 8.1, the lattice parameters '*a*', and '*c*' are increasing with RE substitution up to x = 1.0 composition. The improvement in lattice parameters may be due to the replacement of the smaller Fe^{+3} ions (0.067 nm) by the bigger La^{+3} (0.106 nm), and Sm^{+3} (0.096 nm) ions [Luo *et al*. (2015), Auwal *et al*. (2016a)]. With the substitution by the RE ions, the crystal plains distance increases and results crystal lattice enlargement, i.e., lattice parameter (LP) is increased. The decrease in lattice parameters for x = 1.5 composition may be due to the presence of secondary phase (SmFeO$_3$). The other reason may be that the size of the octahedral site is larger than the tetrahedral site in the matrix. The ionic radius of the RE ion is much bigger for the octahedral site. It may be assumed that a small amount of RE cations may be substituted by Fe^{+3} cations. It may go into the octahedral sites by redistribution of the ions between the octahedral and tetrahedral sites to reduce the free energy of the matrix. It may be that there is a partial relocation of ions from B to A sites at

the octahedral sites accompanied by an opposite transfer of equivalent number from A to B sites in order to relax the strain. Therefore, the lattice constant decreases.

'*c/a*' ratio in all the compositions is less than 3.98, which can be used to measure the structure of the hexaferrite [Wagner *et al*. (1998), Auwal *et al*. (2016a)]. The crystallite size is increased with the substitution up to x = 1.0. The enhancement in the crystallite size may be due to the substitution of smaller ions by the larger RE ions. This replacement may cause an internal tensile strain to create the lattice distortion, and results in an enhancement of the crystallite size. The crystallite size is decreased for x = 1.5 composition, it may be due to the presence of secondary phase. It could be explained that Sm^{+3}, and La^{+3} ions may diffuse to the grain boundaries during sintering. They suppress the grain growth, and restrains its motion, which leads to the decrease in the crystallite size [Liu *et al*. (2011), Luo *et al*. (2015)].

Table 8.3 Bulk density, Theoretical density and grain size with EDX analysis of sintered $SrAl_4(La_{0.5}Sm_{0.5})_xFe_{8-x}O_{19}$ samples.

Composition	Density (g/cm^3)	Theoretical density	Grain Size (μm)	Elemental composition (At%)				
				Sr	Al	La	Sm	Fe
x = 0.0	5.08	5.10	1.11	4.07	15.19	-	-	34.31
x = 0.5	5.12	5.14	1.18	4.01	14.91	0.23	0.19	30.97
x = 1.0	5.28	5.30	1.31	3.96	15.01	0.41	0.28	29.15
x = 1.5	5.11	5.14	1.02	3.99	14.96	1.09	0.89	27.78

Table 8.3 shows the bulk density along with the grain size, and elemental analysis of La-Sm substituted Sr ferrite. Bulk density is increased continuously up to x = 1.0. The improvement in density with RE ions can be ascribed to the atomic weight of La^{+3} (138.9),

and Sm^{+3} (150.3), which are larger than those of Fe^{+3} (55.845). The other reason may be, when the doping is introduced, some trivalent Fe^{+3} ions are replaced by RE ions in the grain boundary (GB) area, so the quantity of metal ion vacancies in the surrounding area is increased in order to keep the equilibrium of the electric charges, which may result in the enhancement of the GB movement speed. Therefore, the grain size of the ferrite is increased with substitution [Fu *et al*. (2011)]. The reduction in density for x = 1.5 composition may be due to the occurrence of secondary phases, which suppress grain boundary mobility during sintering process [Greskovich and Lay (1978)].
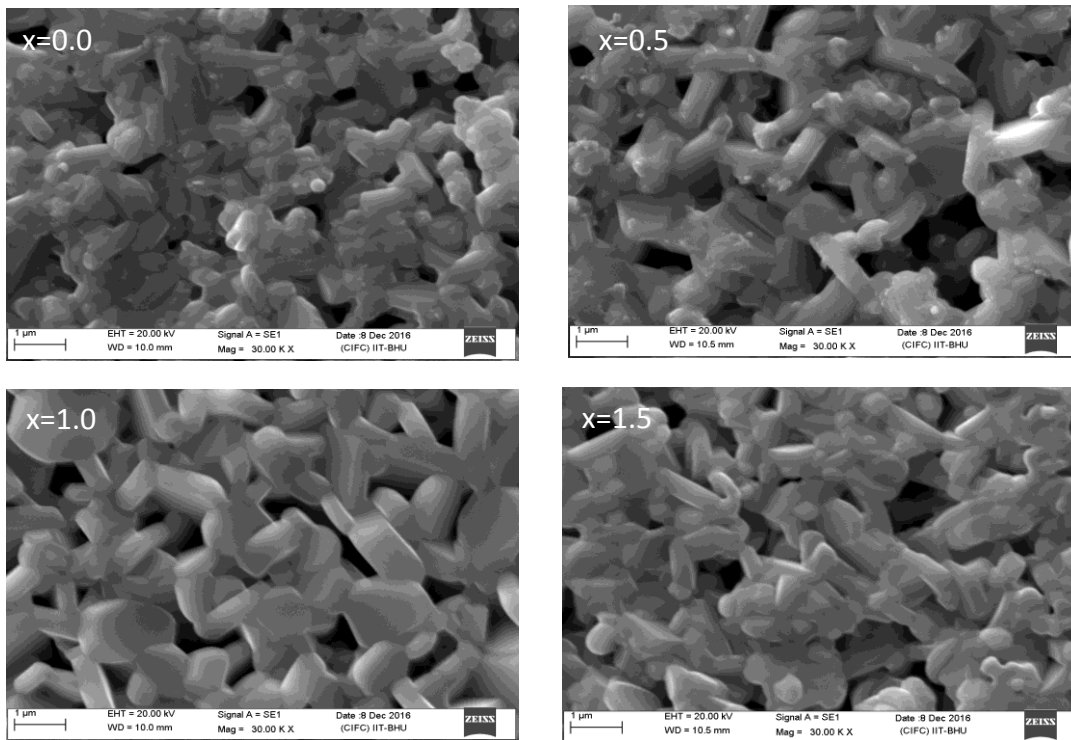
Figure 8.4 SEM micrograph of sintered $SrAl_4(La_{0.5}Sm_{0.5})_xFe_{8-x}O_{19}$ hexaferrites.

The microstructure of the sintered ferrite examined by SEM is shown in Figure 8.4. It is observed that the grains are homogeneous, and closely packed throughout the matrix. The grains have platelet-like morphology, and grain growth along the *c*-axis. It is desirable for the magnetic properties in Sr ferrite [Kim *et al*. (2016)]. The increase in grain size with

increasing doping content is clearly seen in Figure 8.4. The decrement in grain size for x = 1.5 composition is mainly due to the presence of a secondary phase, which hinders the grain growth, as reported earlier also [Rai *et al*. (2013a)]. To achieve the proper balance between two desirable properties (i.e., *Br* & *iH$_c$*) grain size should be in between 1-2 μm [Huang *et al*. (2017)].
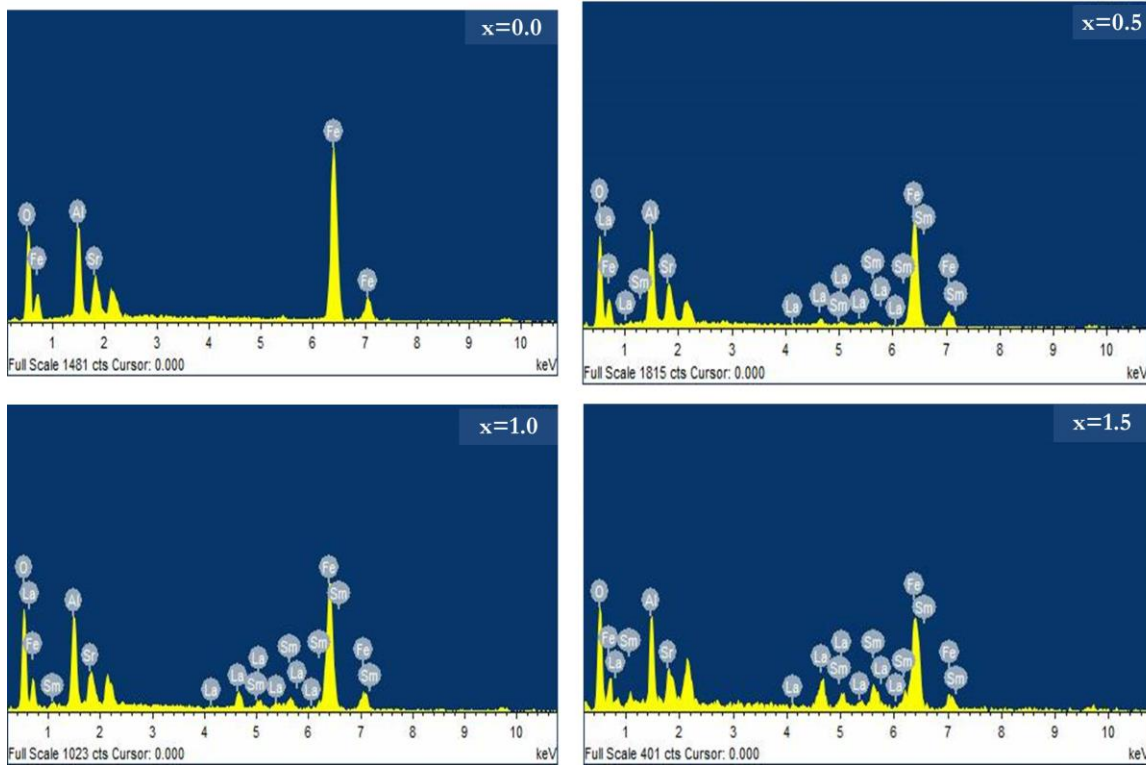

Figure 8.5 EDX micrograph of sintered $SrAl_4(La_{0.5}Sm_{0.5})_xFe_{8-x}O_{19}$ hexaferrites.

To confirm the elemental composition of prepared $SrAl_4(La_{0.5}Sm_{0.5})_xFe_{8-x}O_{19}$ hexaferrites, EDX analysis is carried out. Figure 8.5 shows the EDX micrograph of sintered $SrAl_4(La_{0.5}Sm_{0.5})_xFe_{8-x}O_{19}$ hexaferrites and corresponding elemental atomic percentage (At%) are presented in Table 8.3. With substitution, At% of La and Sm increase while, Fe decreases. The elemental mapping of Sr, Al, La, Sm and Fe is homogeneously distributed at all the places in the sintered sample, as shown in Figure 8.6, respectively. At x = 1.5,

secondary phase of $SmFeO_3$ is detected in $SrAl_4(La_{0.5}Sm_{0.5})_{1.5}Fe_{6.5}O_{19}$ hexaferrite. So, elemental mapping shows the presence of secondary phase that is also confirmed by XRD analysis of $SrAl_4(La_{0.5}Sm_{0.5})_{1.5}Fe_{6.5}O_{19}$ hexaferrite.
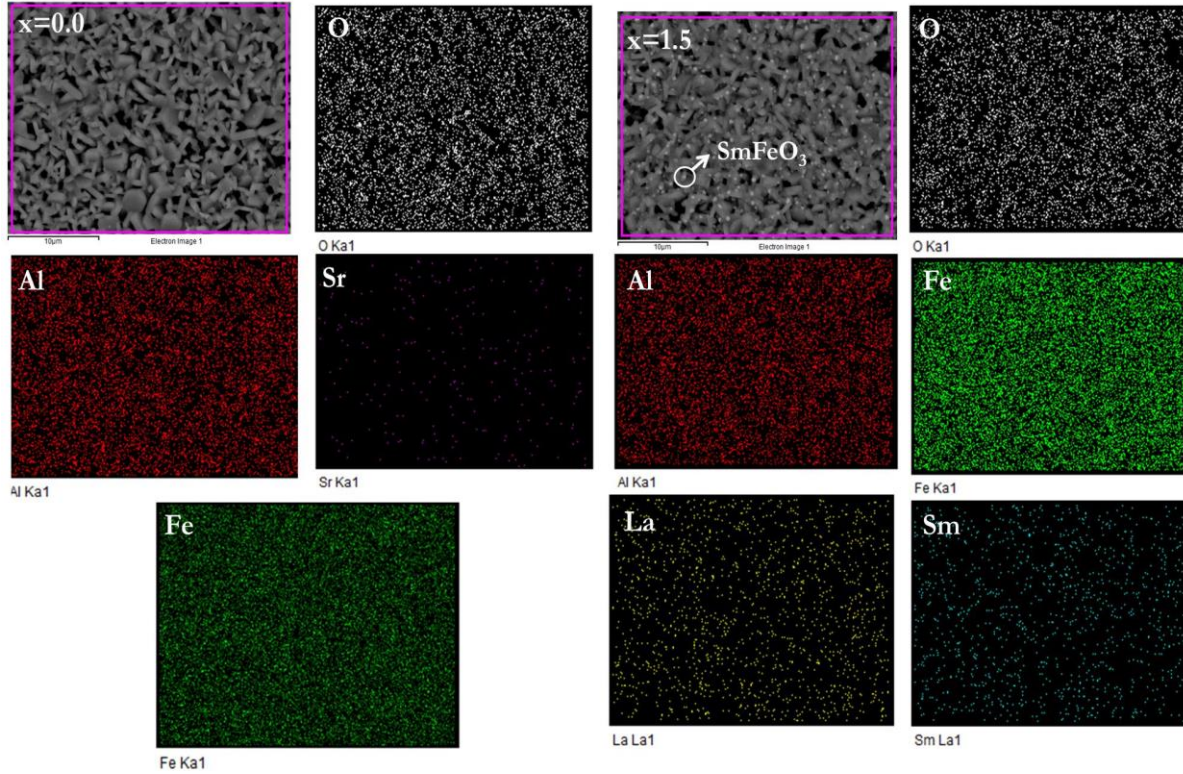

Figure 8.6 Elemental mapping of sintered $SrAl_4(La_{0.5}Sm_{0.5})_xFe_{8-x}O_{19}$ hexaferrites with x = 0.0 and 1.5.

Figures 8.7 to 8.11 have manifested the magnetic behavior of sintered samples. Figure 8.7 shows the *M-H* curve of the synthesize $SrAl_4Fe_{(8-x)}(La_{0.5}Sm_{0.5})_xO_{19}$ hexaferrites. The alteration of remanent magnetization (*Br*) with bulk density is shown in Figure 8.8 as a function of La & Sm content. Magnetic properties of Sr ferrite are a mixture of intrinsic, and extrinsic properties. Intrinsic properties, i.e., M_s mostly depends on site occupation of doping cations (composition), bulk density, and magnetic moment [Cui *et al*. (2014)]. From the Table 8.3, it is shown that RE ions are improving the density of sintered sample up to x = 1.0.

It causes to enhance the magnetic dipole per unit volume, therefore, M_s and M_r increase with the substitution. Increasing of saturation magnetization (M_s) of the system hence, *Br* increases with La, and Sm content up to x = 1.0.
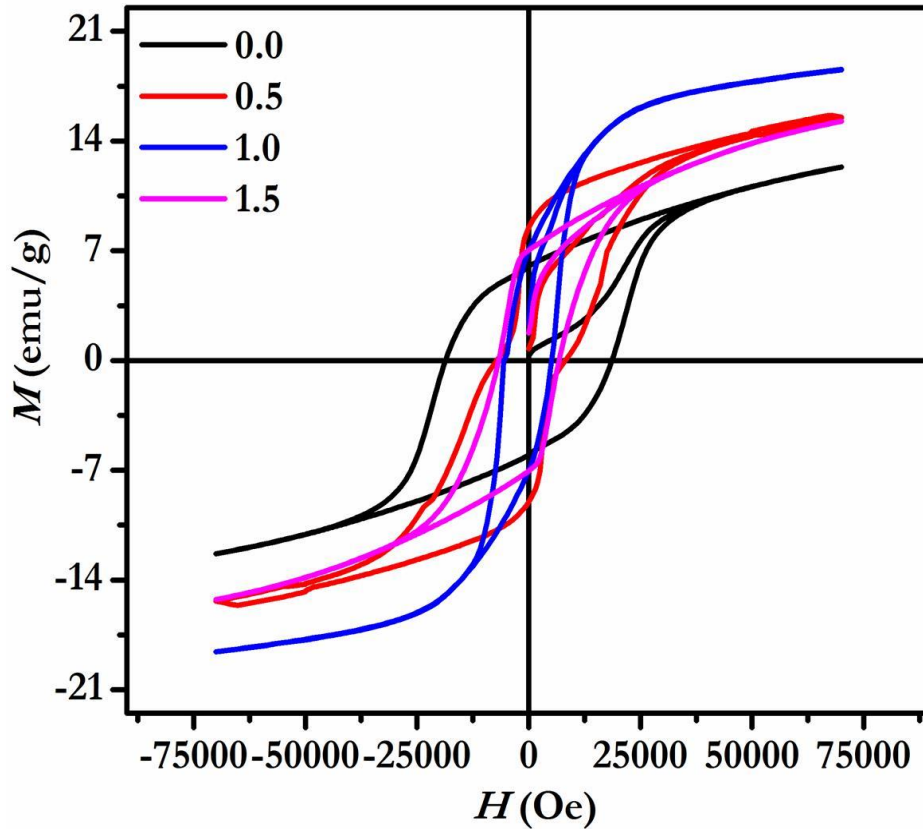

Figure 8.7 Hysteresis loops as a function of the La & Sm concentration.

Table 8.4 summaries all the magnetic parameters with function of La and Sm content. The Bohr magneton shows that it is increased with RE content. The upward trend of ramnance magnetization (Figure 8.8) may be attributed to the improvement of grain size. Rare earth element may prefer to reside in the octahedral site (*12k*, *2a*, *4f₂*) due to the volume effect [Liu *et al*. (2011)]. Auwal *et al*. (2016a) have reported that La^{+3} rare earth preferentially occupies (*4f₂*) site, and Ashraf *et al*. (2018) also have claimed that lower doping concentration of Sm^{+3} may prefer *4f₂* site. Strontium hexaferrite contains 5 sites of

Fe^{+3} ions, such as three octahedral site among which (*12k*, *2a*) with spin up direction, and (*4f$_2$*) spin down direction, one tetragonal site (*4f$_1$*) with spin down direction, and one trigonal bipyramidal site (*2b*) with spin up direction [Uestuener *et al.* (2006)].

Table 8.4 *Br*, Bohr magnetron (μ_B), *iH$_c$*, *bH$_c$*, *H$_k$/iH$_c$,(BH)$_{max}$* and Tc of sintered $SrAl_4Fe_{(8-x)}(La_{0.5}Sm_{0.5})_xO_{19}$ samples.

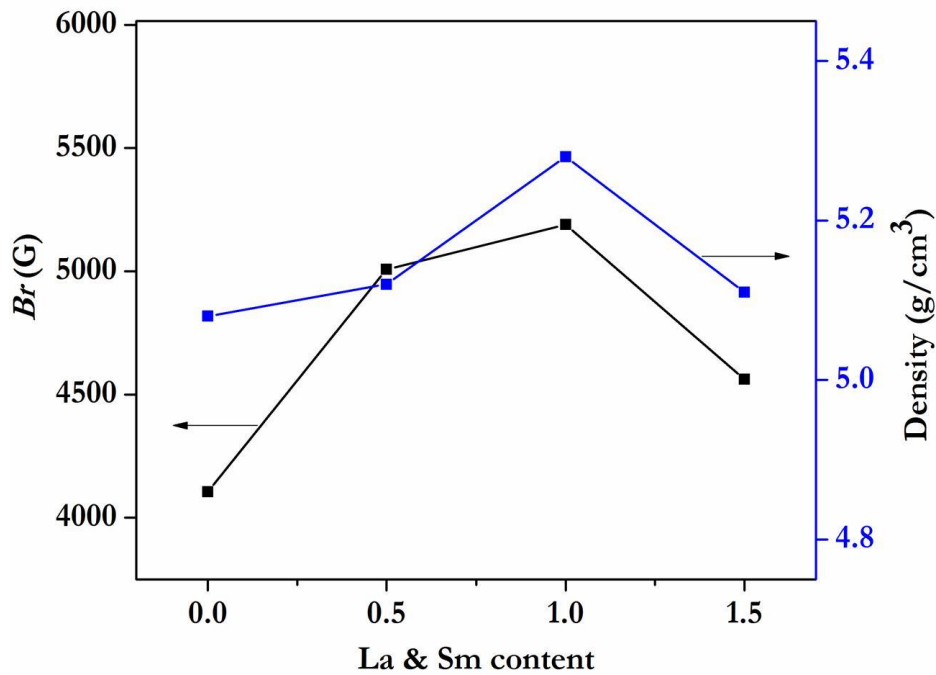| Composition	*Br* (G)	Bohr magneton (μ_B)	*iH$_c$* (kOe)	*bH$_c$* (Oe)	*H$_k$/iH$_c$*	*(BH)$_{max}$* (MGOe)	Tc (°C)
x = 0.0	4105.88	4.02	18.15	18.02	0.89	6.03	320
x = 0.5	5007.53	4.30	6.25	6.05	0.87	6.28	220
x = 1.0	5189.76	4.57	6.17	6.02	0.86	6.69	219
x = 1.5	4561.56	4.51	6.23	6.11	0.91	5.42	193

Figure 8.8 Remanence *Br* and bulk density as a function of the La & Sm concentration.

At ($4f_2$) site, Fe with spin down moment has been replaced by the rare earth elements, which contain the lower magnetic moment (Sm^{+3} and La^{+3} have 1.5 μ_B and 0 $\mu_{B,}$ respectively) as compared to Fe^{+3} ($5\mu B$), results the increase in overall magnetic moment hence, the total magnetization of hexaferrite. The further decrement of magnetization may be due to the higher concentration of RE ions which steadily alter the magnetization from collinear spin to non-collinear spin of Fe^{+3} ion. It has also been reported that substitution by rare earth element can decrease the strength of super-exchange interaction between Fe^{+3}-O-Fe^{+3}, which leads to non-collinear or spin-canting arrangement of magnetic moments [Sadiq *et al*. (2015)]. It may also be due to the development of the secondary phase of $SmFeO_{3,}$ as noticed in XRD study [Ashraf *et al*. (2018)].
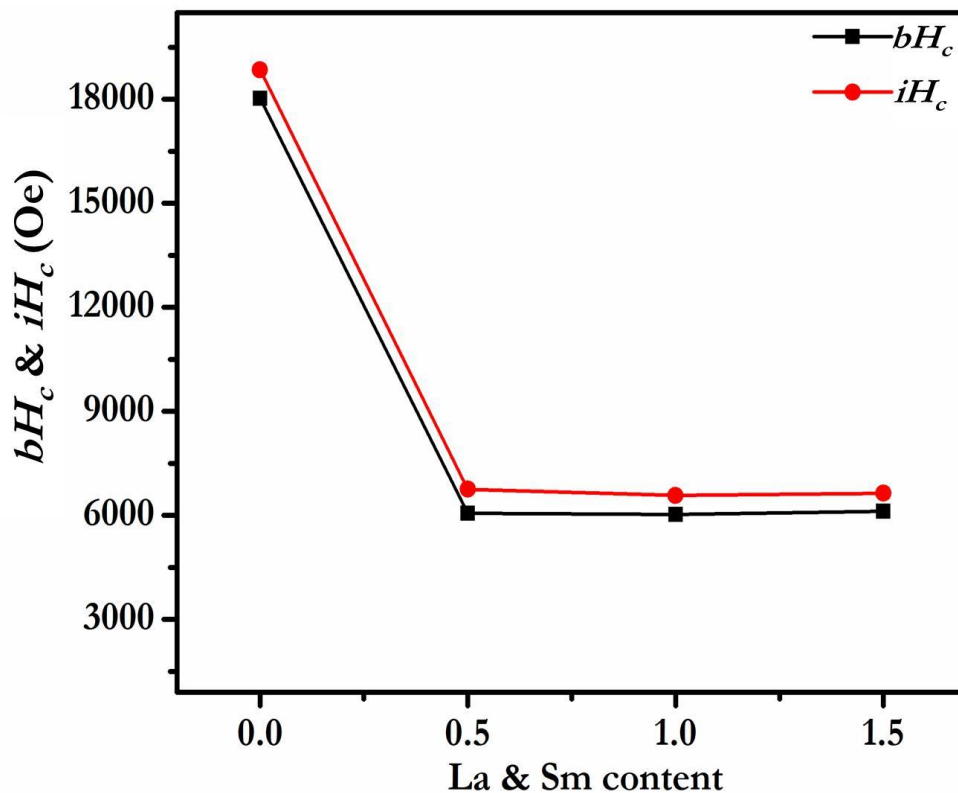

Figure 8.9 Magnetic induction coercivity (bH_c) and intrinsic coercivity (iH_c) as a function of the La & Sm concentration.

From Figure 8.9, it is found that the coercivity (iH_c and bH_c) decreases gradually with composition up to x = 1.0. It may be due to morphology and magneto-crystalline anisotropy. The bH_c (magnetic induction coercivity) is the magnetic field, which causes the induction (B) allocation in the magnet to alter its direction. It is normally lesser than iH_c (intrinsic coercivity). The decrement in iH_c is due to the increase in grain size. From the Table 8.3, it has been observed that the grain size is continuously increased with substitution. The increments of grains are responsible for decreasing the grain boundaries that contribute to the obstruction of domain wall motion, thus decreasing the coercivity [Hooda *et al*. (2015)]. The improvement in coercivity for x = 1.5 composition may be due to a decrease in grain size. In this work, subsequent improvement in ramnance magnetization is achieved without very much reducing in coercivity.
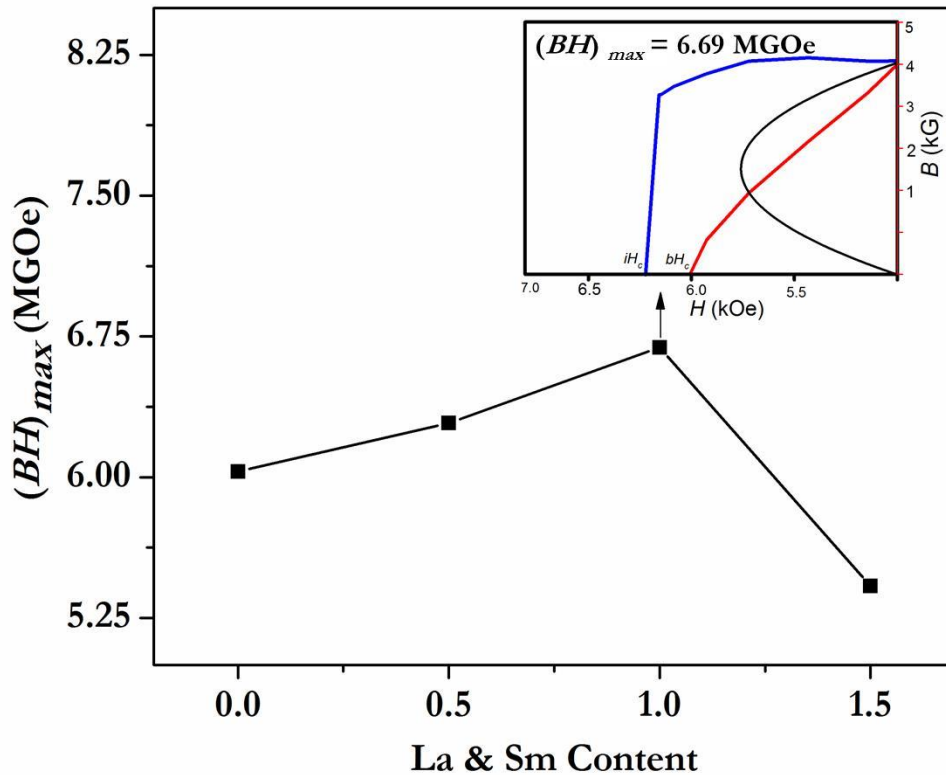

Figure 8.10 Maximum energy product *(BH)$_{max}$* as a function of the La & Sm concentration.

Table 8.4 shows the ratio of H_k/iH_c, which is one of the important magnetic properties of hexaferrites. It is observed that the ratio is decreased up to x = 1.0 composition. It may be due to the varying trend of intrinsic coercivity (iH_c) of the ferrites. In addition, if the values of the H_k/iH_c ratio is >0.85, usually considered for squareloop ferrite, i.e., permanent magnet.

Figure 8.10 shows the energy $(BH)_{max}$ with the function of La and Sm content. It is increased up to x = 1.0, then it is decreases with substitution. The maximum value 6.69 MGOe is achieved for x = 1.0 composition. It can be found that the varying trend of the energy of the ferrite is in harmony with remanence magnetization (Br). The value of $(BH)_{max}$ is much higher than the previously reported value for Sm (30 kJ/m^3 ~ 3.77 MGOe) [Yang *et al*. (2018)] & La (28.4 kJ/m^3 ~ 3.57 MGOe) [Liu *et al*. (2006)].

Table 8.4 shows the Curie temperature values of substituted hexaferrites. It decreases with increasing RE substitution. Substitution of Fe by RE ions, creates a deviation of the co-linear arrangement of magnetic moments resulting in so-called spin canting structure [Liu *et al*. (2006)]. Spin canting structure is responsible for the decrease of Tc (Curie temperature) with increasing substitution. The decrease of Curie temperature with substitution may also be due to a decrease of exchange interaction between Fe ions, as RE elements enter the lattice and/or because crystalline disorder increases with substitution.

Figure 8.11 & 8.12 show the dielectric properties of sintered ferrites for understanding the electrical behavior of the material. The values of dielectric constant ($\mathcal{E}$) and AC resistivity (ρ) of $SrAl_4(La_{0.5}Sm_{0.5})_xFe_{8-x}O_{19}$ ferrites at 1 MHz is tabulated in Table 8.5. Figure 8.11, shows the graph between $\mathcal{E}$ with frequency. It is observed that $\mathcal{E}$ decreases with the frequency in all the samples. This is a common behavior of dielectric response, which is reported by many investigators in RE substituted Sr-ferrites [Smit and Wijn (1959), Want *et*

al. (2015)]. This entire fact can be described on the basis of Koops theory [Koops (1951)].

He has suggested that the mixed nature of the ferrites consist of conducting grains, and

highly resistive grain boundaries having different dielectric and thickness of grains.

Table 8.5 Dielectric constant, and resistivity of sintered $SrAl_4(La_{0.5}Sm_{0.5})_xFe_{8-x}O_{19}$

ferrites at 1 MHz.

Composition	Dielectric constant (ε)	Resistivity (ρ) *10^4 (Ω-cm)
x = 0.0	20.52	5.54
x = 0.5	24.97	2.78
x = 1.0	25.95	2.11
x = 1.5	12.18	3.45
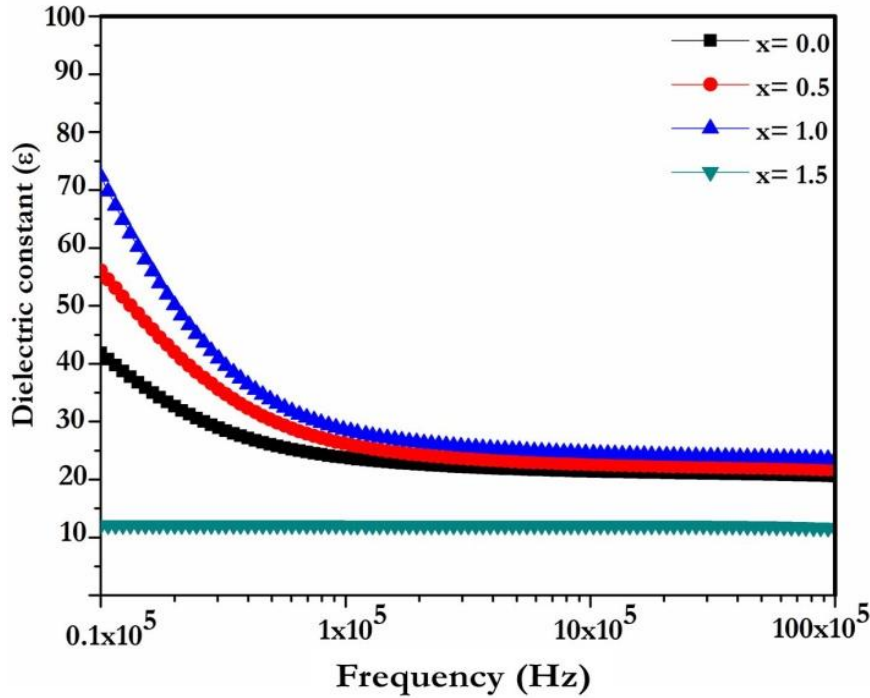
Figure 8.11 Plots of dielectric permittivity versus frequency of
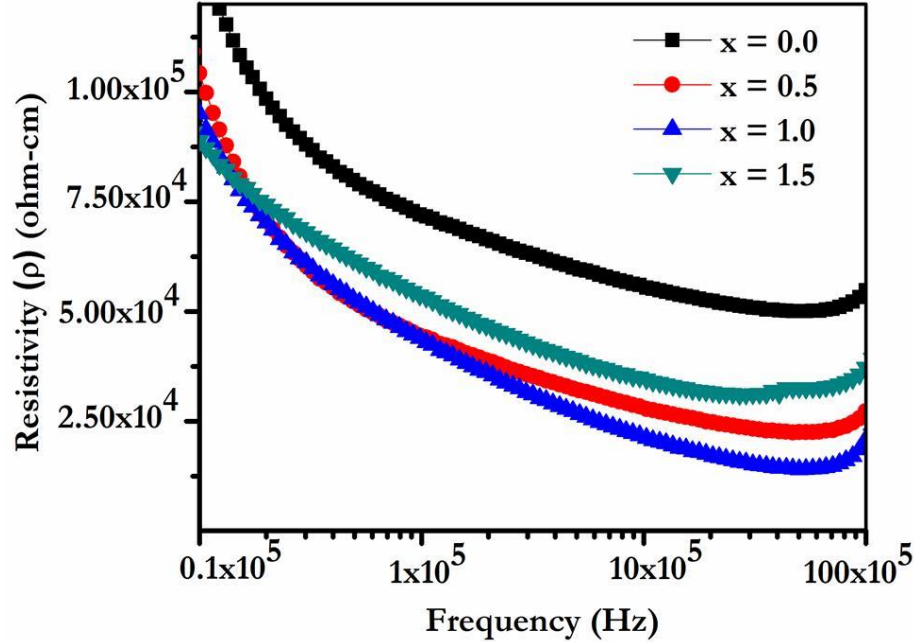
$SrAl_4Fe_{(8-x)}(La_{0.5}Sm_{0.5})_xO_{19}$ ferrites.
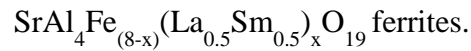
Figure 8.12 Variation of AC resistivity with frequency of $SrAl_4Fe_{(8-x)}(La_{0.5}Sm_{0.5})_xO_{19}$ ferrites.

Grain has a lower dielectric constant due to low resistivity. The larger value of dielectric constant at lower frequency may be due to dislocations, voids, and other defects like porosity [Sirdeshmukh *et al*. (1998)]. The ε is increased with substitution. This enhancement in dielectric constant with doping can be explained by the grain size. As tabulated in Table 8.3, grain size is increased with La^{+3} and Sm^{+3} substitutions. The dielectric constant mainly depends on the population and mobility of domain walls [Mudinepalli *et al*. (2015)]. Increases the grain size leads to reduce the grain boundary, consequently decreasing the restriction in domain wall motion. Therefore, enhances the dielectric constant with substitution.

Figure 8.12 shows the graph of AC resistivity (ρ) with frequency. All the samples show a decrease in ρ with the increase in frequency. From Table 8.5, it can also be found that

the ρ decreases with increasing substitution up to x = 1.0. The decrease in resistivity may be due to an increase in grain size (Table 8.3). The bigger grains have a less number of GB. Grain boundaries are dislocated areas with full of imperfections, i.e., porosity, dislocations, and other secondary phases, which are associated with grain boundaries. The grain boundaries are highly resistive and causes a decrease in resistivities. Further, reduction of iron ions at the higher substitution of rare earth ions decrease the number of hoping electrons thereby increasing the resistivity of the samples.

8.3 Summary

The La and Sm substituted strontium hexaferrite $SrAl_4(La_{0.5}Sm_{0.5})_xFe_{8-x}O_{19}$ (0≤ x ≤1.5)) have been successfully synthesized by the auto combustion method. The XRD study reveals the formation of a M-type hexagonal structure with minor $SmFeO_3$ secondary phase. Lattice parameters and crystallite size increase with the increase in La and Sm content in the sample. Rietveld refinement reveals that all the samples have hexagonal crystal symmetry with *P63/mmc* space group. The lattice strain increases with the increase in La and Sm concentration due to the larger ionic radius of RE ions, which substitutes Fe^{+3} ions in the lattice. Intrinsic coercivity (*iH_c*) has been observed to decrease up to 6.175 KOe due to an increase in grain size with La and Sm inclusion. However, ramnance (*Br*) and *(BH)_max* increase up to 5.18 KG and 6.69 MGOe, respectively for x = 1.0 composition. The dielectric constant for doped samples shows frequency dispersion at lower frequencies, which decreases significantly at higher frequencies. The resistivity is decreased up to 2.11×10^4 Ohm-cm (at 1 MHz). The optimized properties are obtained from x = 1.0 composition.